Fungus-initiated catalytic reactions at hyphal-mineral interfaces drive iron redox cycling and biomineralization

Guang-Hui Yu [a,b,*], Zhi-Lai Chi [b,c], H. Henry Teng [a,d], Hai-Liang Dong [e,f]
Andreas Kappler [g], Michael R. Gillings [h], Matthew L. Polizzotto [i], Cong-Qiang Liu [a]
Yong-Guan Zhu [j,k,*]

[a] Institute of Surface-Earth System Science, Tianjin University, Tianjin 300072, China
[b] Tianjin Key Laboratory of Earth Critical Zone Science and Sustainable Development in Bohai Rim, Tianjin University, Tianjin 300072, China
[c] College of Resources & Environmental Sciences, Nanjing Agricultural University, Nanjing 210095, China
[d] Department of Chemistry, George Washington University, Washington, DC 20006, USA
[e] State Key Laboratory of Geobiology and Environmental Geology, China University of Geosciences, Beijing 100083, China
[f] Department of Geology and Environmental Earth Sciences, Miami University, Oxford, OH 45056, USA
[g] Geomicrobiology, Center for Applied Geosciences, University of Tuebingen, Tuebingen 72076, Germany
[h] Department of Biological Sciences, Macquarie University, Sydney, New South Wales 2109, Australia
[i] Department of Earth Sciences, University of Oregon, Eugene, OR 97403, USA
[j] Key Lab of Urban Environment and Health, Institute of Urban Environment, Chinese Academy of Sciences, Xiamen 361021, China
[k] State Key Lab of Urban and Regional Ecology, Research Center for Ecoenvironmental Sciences, Chinese Academy of Sciences, Beijing 100085, China

Abstract

The ability of fungi to weather a wide range of minerals influences plant nutrition and enhances global biogeochemical cycles of life-essential elements. The fungus-mineral interface plays a key role in weathering, but the specific mechanisms underlying these processes remain poorly understood. Here, we examined fungal-mineral weathering using hematite and *Trichoderma guizhouense*. We showed that hematite dissolution increased over cultivation time, with the formation of secondary minerals up to ∼3000 μm^{-2} at the interfaces after 66 h cultivation. Of the hematite associated with hyphae, approximately 15% was converted to the secondary mineral ferrihydrite. Importantly, superoxide radicals were detected at the hyphal tips and along the whole hyphae. During cultivation, a high concentration (∼1000 nM) of hydroxyl radical was also detected. Synchrotron radiation based spectromicroscopies at fungus-mineral interfaces suggest that fungus hyphae alter the local redox state of iron and thus are redox-active. These findings indicate that fungus-initiated catalytic reactions occur at hyphal-mineral interfaces, in view of the fact that superoxide does not diffuse far from the site of formation. Furthermore, these results also suggest that the catalytic reactions may serve as a new strategy for microbial iron uptake. Together, these findings constitute a significant step forward in understanding the ways that fungi make minerals available to biological systems.
© 2019 Elsevier Ltd. All rights reserved.

Keywords: Biocatalysis; Fungi weathering; Interfacial process; Mineral dissolution; Superoxides; Synchrotron radiation

---

* Corresponding authors at: Institute of Surface-Earth System Science, Tianjin University, Tianjin 300072, China (G.-H. Yu).

E-mail addresses: yuguanghui@tju.edu.cn (G.-H. Yu), ygzhu@iue.ac.cn, ygzhu@rcees.ac.cn (Y.-G. Zhu).
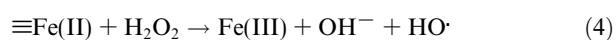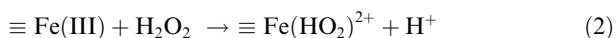
1. INTRODUCTION

Fungi have the ability to weather a wide range of minerals through biomechanical and biochemical processes

(Sterflinger, 2000; Smits et al., 2009; Wei et al., 2012). These bio-weathering processes have important impacts on plant nutrient acquisition (Jongmans et al., 1997) and are likely to have critical roles in the biogeochemical cycling of elements (van Schöll et al., 2008; Hemingway et al., 2018), since one gram of soil can contain hundreds of meters of fungal hyphae (Whitfield, 2007). Biomechanical weathering of minerals proceeds via hyphal penetration and turgor pressure (Bonneville et al., 2016; Li et al., 2016a), whereas biochemical weathering occurs via proton- and ligand-promoted metal mobilization from minerals (van Schöll et al., 2008; Smits et al., 2009). Hypha-promoted mineral dissolution has been recognized as an important process (Banfield et al., 1999; Smits et al., 2009; McMaster, 2012; Ahmed and Holmström, 2015) that could account for 40–50% of bulk bio-weathering (Li et al., 2016a). However, despite their role in bio-weathering, fungi are underappreciated relative to bacteria (Li et al., 2016a), and consequently the processes that mediate hypha-mineral interactions are largely unknown (Gazzè et al., 2012).

Extracellular superoxide (O_2^-) production is widespread in fungi and is involved in lignin degradation, host defense, hyphal branching, and cell differentiation (Aguirre et al., 2005; Rose et al., 2005; Scott and Eaton, 2008). Superoxides play a significant role in the cycling redox-active metals, such as Fe(III) (Fujii et al., 2010). Since redox-active iron minerals are abundant in terrestrial and aquatic systems (Watts et al., 1999; Thompson et al., 2011), they can act as catalysts to promote Fenton-like reactions in the presence of O_2^- (Eqs. (1)–(4)) (Petigara et al., 2002; Garrido-Ramírez et al., 2010; Georgiou et al., 2015).

$$O_2^- + 2H^+ + e^- \rightarrow H_2O_2 \tag{1}$$

$$\equiv Fe(III) + H_2O_2 \rightarrow \equiv Fe(HO_2)^{2+} + H^+ \tag{2}$$

$$\equiv Fe(HO_2)^{2+} \rightarrow \equiv Fe(II) + HO_2\cdot \tag{3}$$

$$\equiv Fe(II) + H_2O_2 \rightarrow Fe(III) + OH^- + HO\cdot \tag{4}$$

where $\equiv$Fe represents the surface of iron oxides. These reactions are different from the classical Fenton reaction (Eq. (5)) where aqueous Fe(II) reacts with hydrogen peroxide (H_2O_2), giving rise to a hydroxyl radical (HO$\cdot$).

$$Fe(II) + H_2O_2 \rightarrow Fe(III) + OH^- + HO\cdot \tag{5}$$
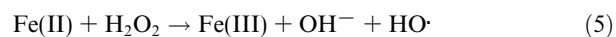
In Fenton-like reactions, aqueous Fe(II) is replaced by redox-active minerals, such as hematite, goethite, and ferrihydrite (Lin and Gurol, 1998; Garrido-Ramírez et al., 2010). Fenton-like reactions are common in natural systems because they can operate over a wide range of pH values, unlike the classical Fenton reaction that operates at a pH of ∼3 (Garrido-Ramírez et al., 2010). Despite the ability of fungi to produce high concentrations of O_2^- (Hansel et al., 2012), the impact of O_2^- on processes occurring at the hypha-mineral interfaces has been largely unexplored. This limits our understanding of this interfacial processes, its impact on microbial dissolution of minerals, and the formation of secondary minerals.

We hypothesized that fungus-initiated catalytic reactions drive mineral dissolution and the formation of secondary minerals at hypha-mineral interfaces. The

objectives of this study were (i) to identify the quantity, composition and location of secondary minerals during biomineralization and (ii) to verify the occurrence of catalytic reactions at hypha-mineral interfaces. We used *Trichoderma guizhouense* NJAU4742 (Zhang et al., 2016) and hematite (Cornell and Schwertmann, 2004; Thompson et al., 2011) as a model fungal organism and mineral, respectively, because they are found in a wide range of environments, including terrestrial and aquatic environments. Additionally, *T. guizhouense* produces considerable amounts of O_2^- in natural environments (Zhang, 2015). Throughout our experiments, advanced techniques of synchrotron-based scanning transmission X-ray microscopy (STXM) images and micro X-ray fluorescence (μ-XRF) as well as stereo microscope were integrated to identify the interfacial processes occurring between fungi hyphae and minerals.

2. MATERIALS AND METHODS

2.1. Preparation of fungal stain and hematite

The experimental fungus *Trichoderma guizhouense* NJAU 4742 was originally provided by Dr. Jian Zhang (Zhang et al., 2016). All experiments were performed in triplicate at 28 °C in the dark using a medium with the addition of hematite to the desired final concentrations. The Potato Dextrose Agar (PDA) medium with an initial pH value of 5.3 contained the followings (per liter): 100 mg of urea, 1400 mg of $(NH_4)SO_4$, 1500 mg of KH_2PO_4, 100 mg of $CaCl_2$ṡ$2H_2O$, 400 mg of $MgSO_4$ṡ$7H_2O$, 100 mg of yeast extract, 5 mg of $FeSO_4$ṡ$7H_2O$, 5 mg of $CoCl_2$, 1.8 mg of $MnSO_4$ṡH_2O, 2.5 mg of $ZnSO_4$ṡ$7H_2O$, 20 g of glucose, and 600 mg of NaCl. Hematite was synthesized by mixing 2 L of 0.002 M HNO_3 (98 °C) with 16.16 g of $Fe(NO_3)_3$-ṡ$9H_2O$ and then aged for 7 d at 98 °C (Schwertmann and Cornell, 2007). After the synthesis of hematite, the suspension was dialyzed with deionized water for 3 d to remove impurities and then the pellets were air-dried.

2.2. Bioweathering experiments

The bioweathering experiments were initiated when the liquid medium containing 0.1% (w/v) hematite was inoculated with *T. guizhouense* conidia (10^4 ml^{-1}) and incubated in a shaking incubator (170 rpm). To prepare the conidial suspension, *T. guizhouense* was grown in a PDA medium for 7 days at 28 °C in an incubator. Fungal biomass was removed by filtration through sterilized muslin cloth, and the filtrates were stored at 4 °C prior to use as conidial suspensions after appropriate dilution with sterile Milli-Q water. The bioweathering experiments were conducted in triplicate using a series of 250 mL Erlenmeyer flasks with 100 mL solution. After cultivating *T. guizhouense* with hematite for 0, 24, 32, 40, 48, 56, and 66 h visible aggregates formed and were filtered through a 0.45 μm polytetrafluoroethylene (PTFE) filter (Xingya Purification Materials Co., Shanghai, China). The filtrates were used for further pH and inductively coupled plasma-atomic emission

spectroscopy (ICP-AES) analyses, respectively. The aggregates after filtration were collected into 1 mL tube.

In addition, contact experiments were conducted by mixing 5 g of minerals into the 5 L medium, followed by inoculation of *T. guizhouense* conidia (10^4 ml^{-1}). Separation experiments followed the same procedure except that the mineral powder was enclosed in a membrane bag (0.22 μm-size) (volume: 10 mL). The flasks containing the final mixtures were incubated in a shaking incubator at 28 °C and 170 rpm for 66 h. Both contact and separation experiments were conducted in triplicate.

2.3. *In situ* detection of O_2^- and the pH of hyphae

Extracellular O_2^- were detected using stains on the PDA solid medium (Hansel et al., 2012). *T. guizhouense* that was grown on PDA plates with an initial pH value of 5.6 were inoculated with Nitroblue tetrazolium (NBT) for detection of O_2^-. The NBT assay employs a mixture of 2.5 mM NBT chloride (Sigma, St Louis, MO, USA) and 5 mM 3-(N morpholino) propanesulfonate-NaOH (a pH of 7.6) to react with O_2^- and forms a blue precipitate upon reaction with O_2^-. PDA plates were subsequently incubated with the NBT solution in the dark for ~30 min. After excess reagents were decanted, and the medium was incubated for additional 12 h. The plates were finally imaged using a stereo microscope (Leica DM 5000B, Leica Microsystems, Germany).

The micro-environmental pH around hyphae growing in the cultivation experiments was measured by confocal laser scanning microscopy (CLSM) with an inverted Zeiss microscope with a Meta510 detector (Zeiss, Jena, Germany) and an argon multiphoton laser at 488 nm. The molecular probe SNARF4F (Invitrogen, Paisley, UK) was used at a 5 μM concentration to determine the pH of the hyphal microenvironments. This molecular probe possesses two specific characteristics of fluorescence emission bands at 580 and 640 nm, respectively, for its acidic and basic forms. By rationing the fluorescence at the two wavelengths, this method becomes independent of the dye concentration, photo-bleaching, and changes of instrumental conditions (Bonneville et al., 2011). A pH-calibration was done by adding 5 μM of SNARF4F to 0.2 mL of a 50-mM phosphate buffer at a pH of 4.6, 5.0, 5.4, 5.8, 6.2, 6.6, 7.0, 7.4, and 7.8 and by calculating the mean value in a histogram of the 547–587 and 619–661 nm channels. After calibration, fungal hyphae were imaged and analyzed.

2.4. Quantification of HO

The samples collected at 0, 24, 32, 40, 48, and 66 h in the bioweathering experiments were used to quantify HO·. The HO· was trapped by terephthalic acid (TPA, non-fluorescent) (Tokyo, Japan), and the fluorescent product, i.e., 2-hydroxyl terephthalic acid (HTPA, fluorescent), was quantitated in an Agilent 1260 Infinity high-performance liquid chromatography (HPLC) system (Agilent Technologies, Inc., Germany) equipped with a Fluorescence Detector (G1321B) and a reverse-phase C18 column (Develosil ODS-UG5, 4.6 mm × 250 mm, Nomura Chemical Co.,

Japan). The concentration of HTPA was used to estimate the cumulative HO· concentration (Li et al., 2004).

2.5. Micro-XRF and STXM analysis at hypha-mineral interfaces

After 66 h of cultivation, the fungal-mineral samples collected in tubes during the mineral dissolution experiments were frozen at −20 °C, followed by sectioning without any embedding. Then, the thin sections (2 μm) were obtained using a cryomicrotome (Cryotome E, Thermo Shandon Limited, Cheshire, UK), transferred to infrared-reflecting MirrIR low-E microscope slides (Kevley Technologies, OH, United States), and analyzed using μ-XRF spectromicroscopy. Chemical images of Fe were collected at the BL15U1 beamline of Shanghai Synchrotron Radiation Facility (SSRF) for the same regions of the thin sections. A fluorescence map (μ-XRF) of Fe was obtained by scanning the samples under a monochromatic beam at E = 10 keV with a step size of 6×8 μm^2 and a dwelling time of 5 s (Sun et al., 2017).

STXM was performed at the BL08U1 beamline of SSRF in Shanghai, China. For STXM image collection, the water-dispersed fungal-mineral aggregates were dropped on the Si_3N_4 window (50 nm thickness), which was installed on the sample holder. After the water evaporated, ratio-contrast imaging of dual-energy absorption for Fe mapping was performed. Three photon energies were chosen: the pre-absorption edge of iron at $E_1 = 706.0$ eV, the absorption edge of Fe(II) at $E_2 = 708.5$ eV, and the absorption edge of Fe(III) at $E_3 = 710$ eV, to scan the sample pixel by pixel (Hunter et al., 2008; Zhang et al., 2010; Jiang et al., 2013).

2.6. Iron K-edge X-ray absorption fine structure (XAFS) analyses

Iron K-edge absorption spectra were collected using a Si (1 1 1) double crystal monochromator at the BL14W1 beamline of SSRF in Shanghai, China. The storage ring was working at 3.5 GeV with 200 mA as an average storage current. The hypha-mineral samples after 66 h of cultivation were filtered using a 0.45 μm PTFE filter and freeze-dried for 72 h. Both the prepared and standard samples of hematite, goethite, ferrihydrite, Fe(III) chloride and Fe (II) chloride were recorded in transmission mode. Fe(III) chloride and Fe(II) chloride represent inorganic complex ferric and ferrous, respectively, whereas hematite, goethite, and ferrihydrite were used as the main iron mineral species. All the samples were mounted in a thin custom-built plastic sample holder covered with Kapton tape and placed at 45° to the incident X-ray beam. Ten scans were averaged for each sample to obtain a good signal-to-noise ratio. The X-ray energy scale was calibrated to the iron K-edge (7112.0 eV) using an iron metal foil before XAFS measurements were performed. The data for an individual X-ray absorption near edge structure (XANES) spectrum were normalized to create a relative intensity value of ~1 for the post edge area of the spectra. Extended X-ray absorption fine structure (EXAFS) spectra were extracted using

the Autobk algorithm (Rbkg = 0.9; k-weight = 3, spline k-range = 3–9 Å^{-1}). A linear-combination fitting (LCF) was performed for both XANES and EXAFS spectra using routine *linearcombo* in the ATHENA software (version 2.1.1) (Ravel and Newville, 2005) using the above 5 standards. The steps of the LCF method have been described previously (Manceau et al., 2012). Briefly, the data were fit to a sum of all five references. Then, references with negative loadings were successively eliminated in ascending order of weight. Next, each reference that had been deleted was added randomly one-by-one, while maintaining the constraint of non-negativity, to ensure that the fit had reached a global rather than local minimum. Uncertainties in the fractions of reference species were discussed previously (Manceau et al., 2012). A standard was considered to have a substantial contribution if it accounted for more than 10% of a linear combination fit.

2.7. Transmission electron microscopy (TEM)

Fungal-mineral aggregates in the mineral dissolution experiments at 4 time intervals (i.e., 0, 24, 48, and 66 h) were dispersed and then dropped onto carbon-coated copper grids for TEM observation after they were air-dried. The images were recorded using a HITACHI microscope (7500, Japan) at an acceleration voltage of 200 keV. The particle-size distribution was calculated using Image J (Li et al., 2016b) (NIH, Bethesda, MD, USA). Briefly, pixel values were first converted into nm using a scale factor. Then, images were converted into binary images and analyzed by "particle analysis" on the ImageJ toolbar (Kumara et al., 2012). High-resolution TEM (HRTEM) images and selected area electron diffraction (SAED) after 66 h of cultivation were conducted using the JEOL JEM-2100F microscope.

2.8. X-ray powder diffraction (XRD) analyses

Reacted fungal-mineral aggregates were freeze-dried at −50 °C for 48 h. Mineralogical identification of freeze-dried samples was carried out using X-ray powder diffraction. Diffraction patterns were recorded from 3 to 85 deg. 2-theta using Ni-filtered Cu K-alpha radiations, and counting 1 s per step, with a step size of 0.02° on a PANalytical X-pert Pro diffractometer using a X-Celerator position sensitive detector.

2.9. Statistical analysis

Differences between the data were assessed with one-way analysis of variance (ANOVA) using the SPSS software version 18.0 for Windows (SPSS, Chicago, IL). Significance was determined using one-way ANOVA followed by Tukey's HSD post hoc tests, where conditions of normality and homogeneity of variance were met. Means ± SE ($n = 3$) followed by different letters in figures and tables indicate significant differences between treatments at $P < 0.05$.

3. RESULTS

3.1. Mineral dissolution and the formation of secondary minerals

After cultivating *T. guizhouense* with hematite for 24 h, a small amount of soluble Fe, defined as the amount of Fe in filtrate after filtration through 0.45 μm PTFE, was detected by ICP-AES (Table 1). After 48 h of cultivation, dissolved Fe was 10 times higher than that at 24 h cultivation (Table 1). A control treatment in which minerals were placed in the medium without *T. guizhouense* did not show any release of Fe (Table 1), ruling out the possibility that abiotic mineral dissolution itself played a role in the release of Fe. A comparison of contact (i.e., allowing the mineral phases to have direct contact with the fungi) and separation (i.e., allowing the mineral phases to interact only with the fungi's products) experiments indicated that direct interaction between fungi and minerals enhanced Fe mobilization by a factor of ~2 (Fig. S1), revealing a critical role of hypha-mineral contact on mineral dissolution.

To characterize the morphology of newly formed secondary minerals, TEM images together with corresponding size-distribution histograms (Fig. 1) were obtained from the fungal-amended medium in the mineral dissolution experiments at four time intervals (0, 24, 48, and 66 h of cultivation). *T. guizhouense* became entangled with hematite after 24 h of cultivation, suggesting a close contact between fungi and minerals. The morphologies of fungus-affected minerals at 48 h and 66 h were distinct from those at 0 and 24 h (Fig. 1a). Specifically, the morphologies of hematite at the former were completely disappeared but still present at the latter. This observation was further supported by both scanning electron microscopy (SEM) and cryo-SEM images (Figs. S2 and S3).

These results indicate a role of fungal activity in mineral dissolution. Large amounts of secondary minerals appeared in and around fungal hyphae (Fig. 1a), with an average size of less than 3 nm (Fig. 1b and Table S1). Additionally, TEM images and corresponding size-distribution histograms showed that the number of secondary minerals increased with cultivation time, up to ~3000 μm^{-2} after 66 h of cultivation (Fig. 1b and Table S1), which was calculated using Image J.

We used XRD (Fig. 2a) to examine the mineralogy after 66 h of cultivation in the mineral dissolution experiments and found that new reflections were identified when compared to hematite only controls. The broad reflection at ~20° suggests the formation of amorphous minerals. To further obtain quantitative information on the different Fe phases present in the hyphae, hypha-mineral samples filtered after 66 h of cultivation were freeze-dried and analyzed using synchrotron-based XAS. The LCF of both XANES and EXAFS analyses showed that the Fe phases associated with hyphae was predominantly hematite (~75%) and ferrihydrite (~15%), with lower amount of inorganic Fe(II) (<5%) and Fe(III) (<5%) (Fig. 2b–c and Fig. S4). These observations support the formation of ferrihydrite at the hypha-mineral interface.

Table 1
Changes of the concentration of dissolved Fe in cultivation experiments.[a]

Treatment	Cultivation time (h)	Fe (mg L^{-1})
Hematite	0	ND
	24	ND
	40	ND
	66	ND
T. guizhouense	0	ND
	24	ND
	40	ND
	66	ND
T. guizhouense + hematite	0	ND
	24	0.06 ± 0.02
	32	0.33 ± 0.08
	40	0.54 ± 0.12
	48	0.75 ± 0.25
	56	0.98 ± 0.13
	66	1.25 ± 0.22

[a] ND: not detected, indicating that the concentration of dissolved Fe was less than 0.01 mg L^{-1}. All experiments were conducted in triplicate. Data are means $\pm$ standard deviation (n = 3).

3.2. Extracellular polymeric substances (EPS) matrix as a sink for secondary minerals

High-angle annular dark-field scanning TEM (HAADF-STEM) clearly indicated the presence of EPS and iron minerals around the cell (Fig. 3a and b). HRTEM images and their corresponding fast Fourier transform (FFT) analyses further showed amorphous or poorly crystalline particles with an interplanar distance of 0.27 nm, suggestive of ferrihydrite (Fig. 3c). Furthermore, SAED pattern analyses indicated poorly crystallized particles with interplanar distances of 0.27 nm, consistent with ferrihydrite (Fig. 3e), but distinctly different from hematite (Fig. 3d).

3.3. Evidence for catalytic reactions at hypha-mineral interfaces

NBT was reduced by O_2^- during *T. guizhouense* cultivation to form blue formazan (Fig. 4a). The location of the formazan precipitate indicated that O_2^- production was in the hyphal tips on the leading growth edge or even along the whole hyphae (Figs. 4a, S5). In addition, O_2^- production was also supported by online detection using continuous flow chemiluminescence (Fig. S6). The pH values of hyphae removed from hematite grains during the mineral dissolution experiments were determined with the fluorescent molecular probe SNARF4F through CLSM. Calibration of the signals revealed a slightly lower pH (5.4–6.2) in the local environment near the cells, suggesting an acidic pH for the hematite-derived samples (Fig. 4b).

Using terephthalic acid as a radical trapper, HO$^·$ can be quantitated by HPLC-fluorescence detection (Li et al., 2004). We found no production of HO$^·$ in hematite-only controls (Fig. 4c). Prior to 48 h, the amount of HO$^·$ production by fungus + hematite cultivation was similar to that by the fungus alone. However, after 66 h the amount was significantly ($p < 0.01$) higher in the fungus + hematite cultivation (1018 ± 200 nM) than in the cultivation of fungus alone (684 ± 49 nM) (Fig. 4c). This difference suggests a role of hematite or newly produced secondary minerals as a catalyst in promoting the production of HO$^·$.

To identify the critical role of Fe minerals in the catalytic reactions, we performed element-specific imaging of samples after 66 h of cultivation. Fig. 5a and b shows the Fe redox heterogeneities at hypha-mineral interfaces where a coating of oxidized Fe, primarily as Fe(III) (i.e., 710 eV/704.5 eV), was distributed at the edges of the hyphae. Moreover, the μ-XRF map (Fig. 5c) showed a heterogeneous distribution of Fe on the surface of the hyphae.

The μ-XANES spectra were collected at the Fe hotspot (i.e., spot with a high Fe concentration) and surface rind of the hyphae (Fig. 5d and e). The intensity of pre-edge peak
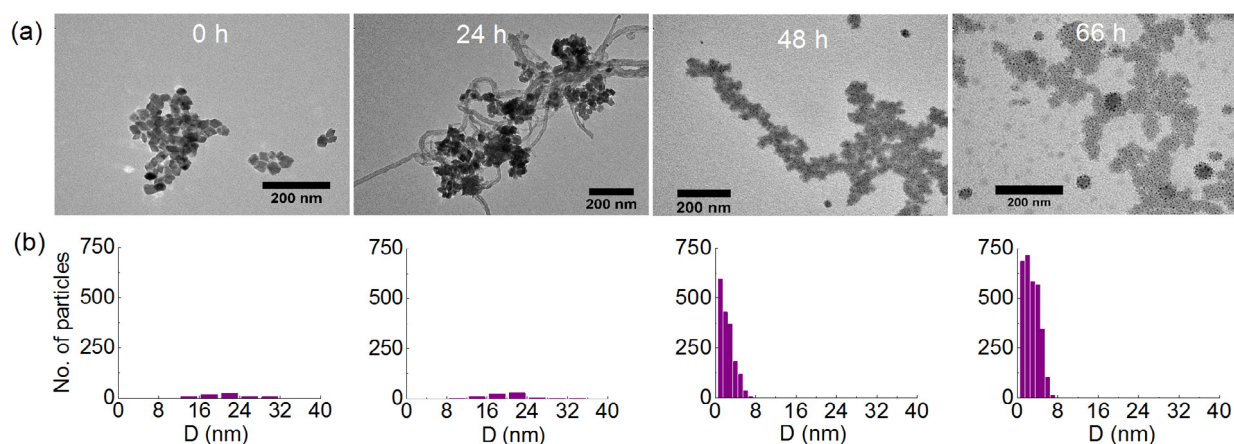

Fig. 1. Time-resolved TEM observations. (a) The formation of nano-scale biogenic minerals during biomineralization. Panels represent typical observations at 0, 24, 48, and 66 h incubation of *Trichoderma guizhouense* with hematite. (b) The corresponding size-distribution histogram analysis. "D" in (b) stands for diameter.
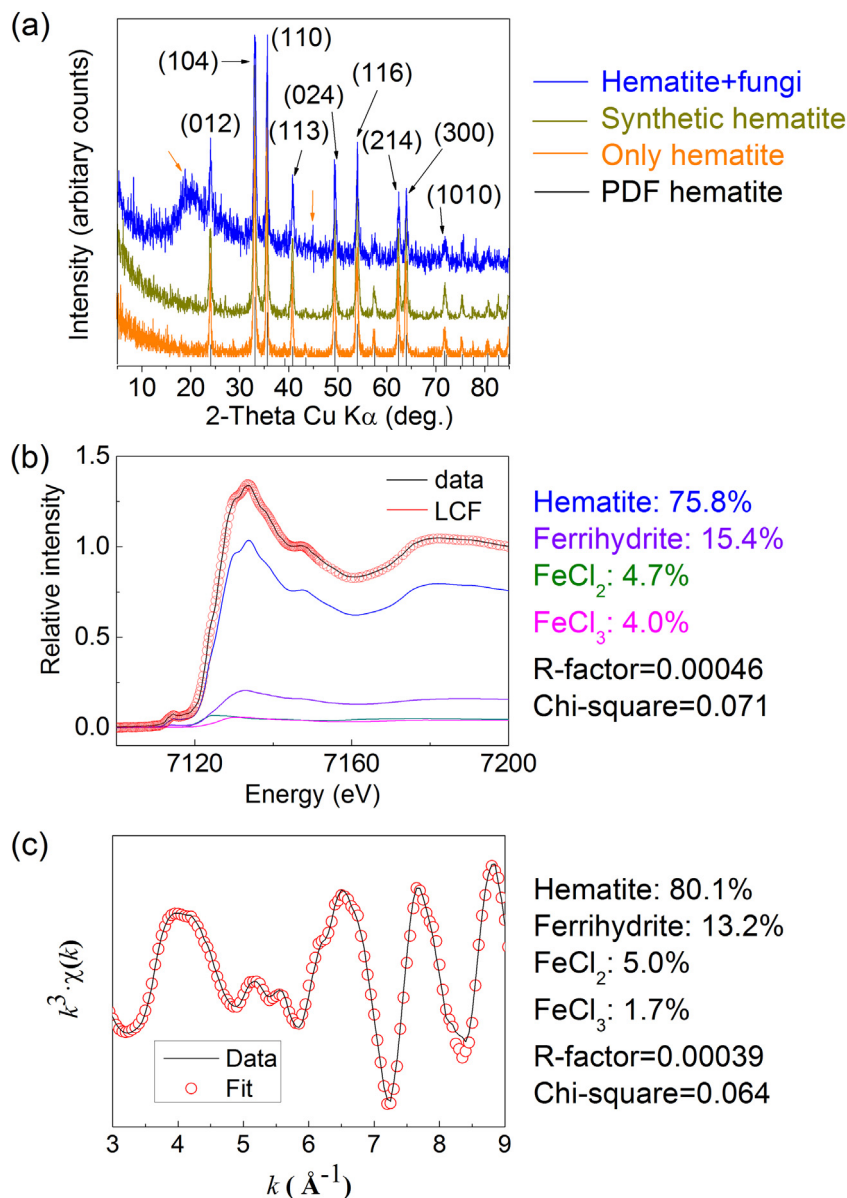
Fig. 2. X-ray powder diffraction and X-ray absorption spectroscopic analysis. Analyses were performed on hypha-mineral samples after 66 h incubation in the mineral dissolution experiments. (a) X-ray powder diffraction pattern. Orange arrows indicate the formation of secondary minerals. (b) Fe K-edge X-ray absorption near-edge structure spectrum. Colored lines represent the separate components for each fit. (c) Extended X-ray absorption fine-structure spectrum. Solid black lines in (b) and (c) represent the k^3-weighted χ-spectra of hypha-mineral samples, and the red circles represent the best fits obtained using linear least-squares fitting. Determination of parameters of fit (R-factor and chi-square) indicated that the linear combination fitting (LCF) results are convincing. (For interpretation of the references to colour in this figure legend, the reader is referred to the web version of this article.)

at ∼7112 eV was lower at the surface rind than that at the hotspot (Fig. 5d). Moving outward from the surface rind to the hotspot, the K-edge peak (∼7127 eV) was substantially decreased in height (Fig. 5d). This lower K-edge peak demonstrated a transition from predominantly oxidized Fe at the surface rind to reduced Fe within the hotspot (Fig. 5d). This transition is further supported by qualitative analysis of the first-derivative XANES spectra indicating a shift in energy between two spectra (Fig. 5e). There is a

shoulder at ∼7137 eV that is not present in the spectrum of the hotspot but is present in the surface rind (Fig. 5d). The distribution of Fe was also supported by the μ-FTIR spectromicroscopy, which further showed a positive but significant correlation between organic functional groups and Fe (Fig. S7). A detailed description of μ-XANES and μ-FTIR spectromicroscopy results is given in the Supplementary Results. Analysis of time resolved Fe(II) in the solution showed that Fe(II) was positively correlated with HO·
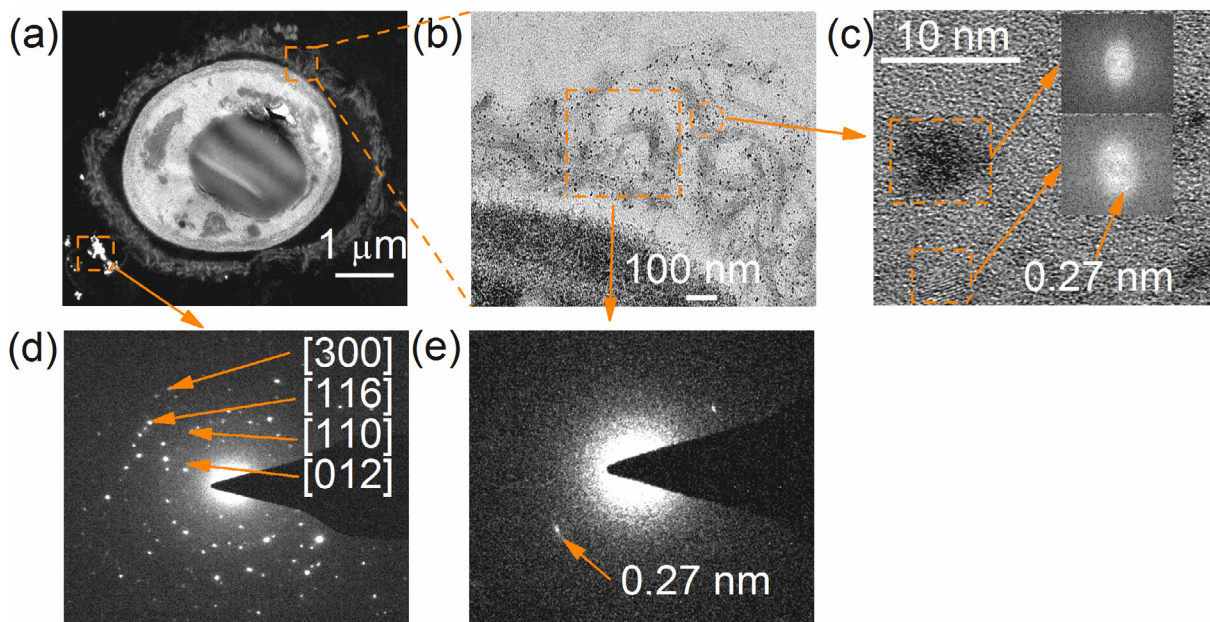
Fig. 3. TEM images of a cross-section (70 nm) after cultivation of hematite for 66 h with *T. guizhouense,* stained with 1% uranyl acetate. Cross sections are shown at different scales (1 µm to 10 nm). (a) High-angle annular dark field scanning TEM (HAADF-STEM) image of a 70 nm section, revealing the presence of EPS and iron minerals around the cell. (b and c) High resolution TEM observations of nanoparticles and their corresponding Fast Fourier Transform (FFT) analyses, showing amorphous or poorly crystallized particles for which the interplanar distance of 0.27 nm corresponds with ferrihydrite. (d) Selected area electron diffraction (SAED) patterns of crystalline hematite, and (e) SAED patterns for poorly crystallized particles.

($R^2 = 0.68$, $p < 0.01$, n = 12) (Tables 2 and S3), indicating that Fe(II) in the solution during biomineralization may be directly related to fungus-initiated catalytic reactions.

We further identified the redox-active substances using differential pulse voltammetry (DPV) (Fig. S8). Fungi and fungal-mineral treatments displayed two similar pairs of DPV peaks that were distinct from those from treatments of minerals alone. The pair with the peak potentials (E_p) at −440 mV (anodic, versus Ag/AgCl), −444 mV (anodic), −416 mV (cathodic), and −420 mV (cathodic) are attributable to flavins, and the pair at $E_p = -122$ mV (anodic), −125 mV (anodic), and −106 mV (cathodic) may be related to outer membrane c-type cytochromes. Moreover, fungal-mineral treatment exhibited a stronger redox peak than fungi alone, suggesting that the presence of hematite may stimulate fungal extracellular electron transfer. This reinforces our findings that nanoscale minerals can facilitate microbial extracellular electron transfer. Additionally, EPS extracts also contained flavins and cytochrome-like substances, as revealed by DPV peaks (Fig. S8).

4. DISCUSSION

4.1. Superoxide and iron chemistry at hypha-mineral interfaces

Superoxide was found to be formed by fungi at the hyphal tips or the whole cell (Figs. 4, S4), which is similar to the previous investigations (Hansel et al., 2012; Tang et al., 2013). Previous investigations indicated that O_2^- could serve as an electron shuttle that increases iron avail-

ability to the microorganism (Fujii et al., 2010). However, high concentration of HO$^\bullet$ in the fungus + hematite cultivation was detected in this study (Fig. 4), which is a strong indicator of the occurrence of catalytic reactions (Eqs. (1)–(4)). In contrast to iron acquisition via siderophores, in this superoxide-mediated Fe-acquisition process microorganisms do not expend energy by release of purpose-built molecules into the environment and as a consequence, this process is likely more efficient, which is revealed by previous reports (Rose et al., 2005; Fujii et al., 2010).

After cultivation of 66 h, the hypha-mineral interface contained approximately 15% of ferrihydrite (Fig. 2b and c), which was further confirmed by HRTEM images and their corresponding FFT analyses (Fig. 3). Dual-energy STXM showed that fungal hyphae were coated by Fe (Fig. 5a and b), suggesting a close contact between hyphae and Fe. This is consistent with the observation from HRTEM images (Fig. 3). Furthermore, both Fe(II) (i.e., 708.5 eV/704.5 eV) and Fe(III) (i.e., 710 eV/704.5 eV) (Hunter et al., 2008; Jiang et al., 2013) were distributed on the surface of the hyphae (Fig. 5a and b). The μ-XANES spectra were further collected (Fig. 5d and e), with the pre-edge peak at ∼7112 eV, assigned to the 1s → 3d transition, being focused, owing to its sensitive to the geometry of the Fe atom (Garcia-Prieto et al., 2016). The intensity of the pre-edge peak at the surface rind was lower than that at the hotspot (Fig. 5d), indicating a more centrosymmetric environment for Fe at the surface rind than within the hotspot. Meanwhile, the K-edge peak (∼7127 eV) of Fe, assigned to the 1s → 4p transition, was lower at the
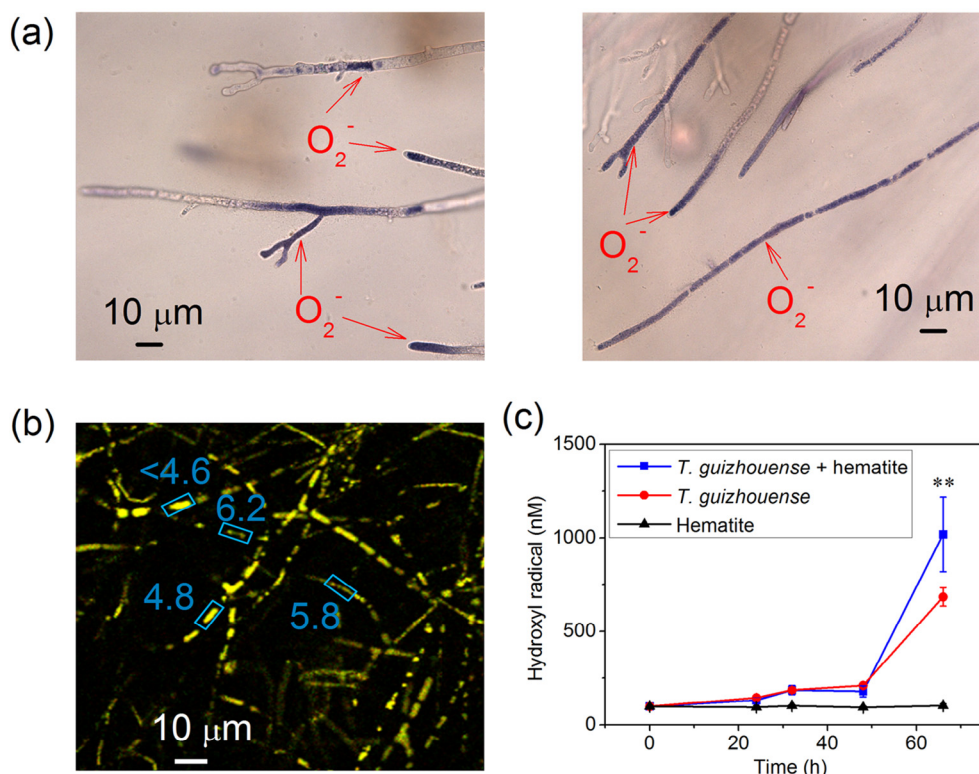
Fig. 4. Superoxide and pH in the hyphae of *T. guizhouense,* and detection of hydroxyl radicals during biomineralization of hematite. (a) Deposits of formazan pigment, indicative of the presence of O_2^- in the tips and growing edges of the fungal hyphae. (b) Micro-environmental pH measurements. Samples were stained with 5 µM SNARF4F (Invitrogen) and measured with confocal laser scanning microscopy using emissions at 580 and 640 nm, after excitation with a 488 nm argon laser. (c) Production of hydroxyl radicals during biomineralization. Concentrations were measured using terephthalic acid and HPLC fluorescence detection. Data are means ± standard deviation (n = 3) (**$p < 0.01$).

hotspot, consisting with a reduced oxidation state of Fe (Berry et al., 2003). The reduced oxidation state of Fe suggests that fungal hyphae may transform oxidized Fe to reduced Fe. In contrast, the shoulder at ~7137 eV was only present in the surface rind (Fig. 5d), suggesting the possibility of the formation of ferritin during the biomineralization of hematite by *T. guizhouense* (Garcia-Prieto et al., 2016). This possibility is also supported by the comparison between Fe K-edge XANES spectra from the surface rind with those of bacterial ferritin (FtnA) and bacterioferritin (Bfr) of *Escherichia coli* and archaeal ferritin (PfFtn) of *Pyrococcus furiosus* (Fig. S9). Specifically, the shoulder at ~7137 eV is present in the spectrum of the surface rind and three native ferritin-like proteins (i.e., FtnA, Bfr, and PfFtn) but is not present in synthetic hematite and ferrihydrite. To summarize, both dual-energy ratio-contrast images and µ-XRF spectromicroscopy demonstrate that fungal hyphae are redox-active, with both ferrous and ferric iron presenting in/around fungal hyphae.

4.2. Proposed conceptual model of fungus-initiated catalytic reactions

Collectively, our cultivation experiments and microscale observations show that a fungus-initiated catalytic reactions drive mineral dissolution and the formation of sec-ondary minerals. This activity occurs at hypha-mineral interfaces, in view of the fact that O_2^- does not diffuse far from the site of formation (Hansel et al., 2012; Tang et al., 2013).

A proposed conceptual model is shown in Fig. 6. Production of O_2^- by fungi at the hyphal tips or the whole cell (Figs. 4, S4) is a critical step (Process 1, Fig. 6) toward mineral dissolution (Table 1) and the formation of secondary minerals (Figs. 1–3). The O_2^-, being a charged species, will rapidly be converted to H_2O_2 through dismutation (Process 2, Fig. 6) (Scott and Eaton, 2008). In the presence of H_2O_2, redox-active minerals (Fig. 2) can act as catalysts or nanocatalysts (Garrido-Ramírez et al., 2010) to promote Fenton-like reactions at hypha-mineral interfaces and produce surface-adsorbed Fe(II) (Process 3, Fig. 6). These nanocatalysts (i.e., new biogenic secondary minerals) are more reactive than catalysts because their active sites are located on the surface (Garrido-Ramírez et al., 2010). As a result, these reactions generate a high concentration of HO˙ (Fig. 4c) and promote the dissolution of Fe(III) minerals via the production of Fe(II) (Table 2). Meanwhile, the produced surface Fe(II) and H_2O_2 (Process 4, Fig. 6) induce Fenton reactions and also form surface Fe(III) as well as HO˙ (Eq. (5)). Since the rate of Fe(III) reduction with superoxide is faster than that of Fe(II) oxidation by superoxide (Melton et al., 2014), superoxide-mediated
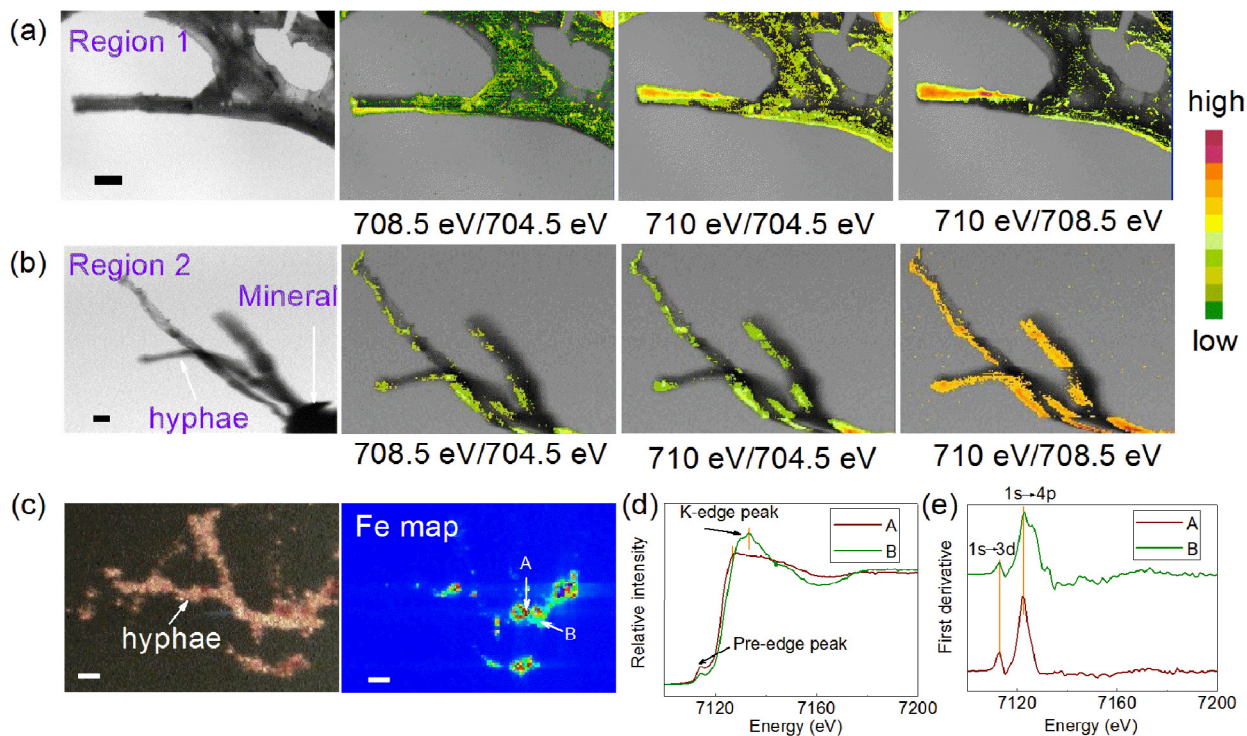
Fig. 5. Redox properties of fungal hyphae. (a and b) Dual-energy ratio-contrast images (with a resolution of 30 nm) acquired near the Fe L_3 edge. (c) μ-XRF spectromicroscopy of the cultivated 66 h hypha-mineral samples. (d) and (e) XANES spectra and their first derivatives, respectively. The color scale is a relative density of Fe species. A and B represent the hotspot of Fe concentration and surface rind region, respectively. Scale bar is 1 μm. (For interpretation of the references to colour in this figure legend, the reader is referred to the web version of this article.)
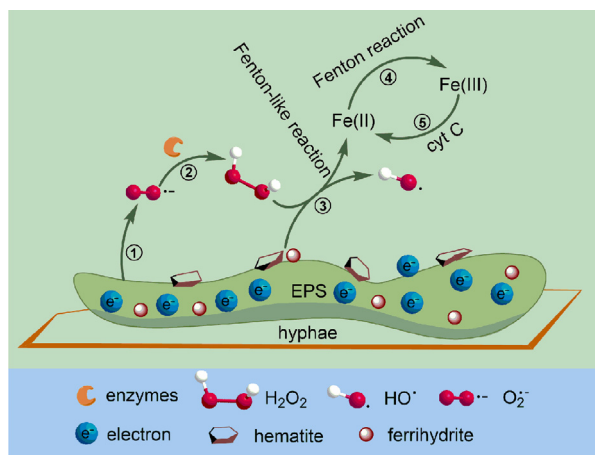

Fig. 6. Conceptual model of fungus-initiated catalytic reactions at hypha-mineral interfaces. Reactions ① → ⑥ represent the processes occurring at hypha-mineral interfaces and are detailed in the main text. ① Production of O_2^- by fungi at the hyphal tips or the whole cell; ② conversion from O_2^- to H_2O_2 by enzymes; ③ Fenton-like reactions; ④ Fenton reaction; ⑤ formation of surface Fe(II) by flavins and c-type cytochromes.

Fenton-like reactions may be dominant when compared to Fenton reaction. The micro-environmental pH measurements (Fig. 4b) also supported the overwhelming advantage

of Fenton-like reactions. Production of HO˙ may be an important strategy to enhance nutrient uptake by fungi, in view of the strong oxidation capability of HO˙ (Williams et al., 2011; Wang et al., 2017). It is evidenced that the production of HO˙ together with proteolysis improved N liberation from proteins in soils (Op De Beeck et al., 2018). In addition, flavins and c-type cytochromes on fungal hyphae (Fig. S6) or a network of EPS (Fig. S7) may directly involved in extracellular electron transfer (Shi et al., 2016; Xiao et al., 2017) and contribute to the formation of surface Fe(II) by interacting with surface Fe(III) (Process 5, Fig. 6). To our knowledge, this is the first study to suggest that fungus-initiated catalytic reactions can occur at hypha-mineral interfaces. These represent a potentially important, but previously unrecognized mechanism for mineral dissolution and the formation of secondary minerals.

4.3. Biogeochemical implications of fungus-initiated catalytic reactions

Given the versatility of O_2^- as a redox reactant and the universal ability of fungi to produce extracellular O_2^- (Rose et al., 2005; Scott and Eaton, 2008; Hansel et al., 2012), this reaction at hypha-mineral interfaces may play a central role in mineral dissolution, biomineralization, nutrient uptake, and the cycling and bioavailability of

Table 2
Time resolved Fe(II) and total Fe during biomineralization (mg L^{-1}).

t (h)	0	24	48	66
Fe(II)	$0.28 \pm 0.05c$	$0.38 \pm 0.11c$	$0.94 \pm 0.11b$	1.34 ± 0.11 a
Total Fe[a]	$0.88 \pm 0.05c$	$1.22 \pm 0.09b$	1.55 ± 0.08 a	$1.28 \pm 0.13b$
Percentage of Fe(II)	$31.8 \pm 0.3\%$	$31.1 \pm 0.1\%$	$60.6 \pm 0.5\%$	$105 \pm 0.8\%$

[a] After reduction of Fe(III) with hydroxylamine chlorhydrate. Significant differences were determined using one-way ANOVA followed by Duncan's multiple range test at $p < 0.05$, in which the conditions of normality and homogeneity of variance were met. All experiments were conducted in triplicate. Data are means $\pm$ standard deviation (n = 3).

redox-active metals (e.g., Fe) in natural systems (van Schöll et al., 2008). Several previous investigators found that at hypha-mineral interfaces, biomechanical forces of hyphal growth played an important role in fungal weathering, which may breach the mineral lattice (Bonneville et al., 2016; Li et al., 2016a). Because biomechanical forces coexisted with exudate-induced chemical weathering, we suggest that fungal-initiated catalytic reactions may be more critical than biomechanical forces in mineral dissolution that occur at hypha-mineral interfaces.

Iron is the most abundant of the transition metals at 6.7 wt% in the continental crust (Rudnick and Gao, 2004). In many cultivated soils, Fe is a relatively abundant element with a total concentration of 20–40 g kg^{-1} (Cornell and Schwertmann, 2004). Accordingly, mobilization of Fe by fungi can contribute to global nutrient cycling budgets. Furthermore, these catalytic reactions may be useful for fungi to exhibit anti-bacterium activity, by producing strongly oxidants (i.e., HO$^\cdot$) (Williams et al., 2011). However, the production of strong oxidants could also be fatal to fungi (Wang et al., 2017). Previous reports have shown that the biogenic Fe minerals could protect microbes from ultraviolet radiation (Gauger et al., 2015). Our results in this study showed for the first time that radical capture through these catalytic reactions that consume oxidants by biogenic minerals may serve as a protective mechanism for fungi. Most importantly, this catalytic reaction can also be expanded from sunlit environments into dark environments, including wetlands, soils, and sediments, owing to the ubiquity of fungi in these environments (Whitfield, 2007) and thus the production of superoxide not restricted to sunlight (Diaz et al., 2013; Melton et al., 2014).

ACKNOWLEDGEMENTS

APPENDIX A. SUPPLEMENTARY MATERIAL

Supplementary data to this article can be found online at https://doi.org/10.1016/j.gca.2019.06.029.

REFERENCES

Aguirre J., Ríos-Momberg M., Hewitt D. and Hansberg W. (2005) Reactive oxygen species and development in microbial eukaryotes. *Trends Microbiol.* **13**, 111–118.

Ahmed E. and Holmström S. J. M. (2015) Microbe-mineral interactions: the impact of surface attachment on mineral weathering and element selectivity by microorganisms. *Chem. Geol.* **403**, 13–23.

Banfield J. F., Barker W. W., Welch S. A. and Taunton A. (1999) Biological impact on mineral dissolution: application of the lichen model to understanding mineral weathering in the rhizosphere. *Proc. Natl. Acad. Sci. USA* **96**, 3404–3411.

Berry A. J., O'Neill H. S. C., Jayasuriya K. D., Campbell S. J. and Foran G. J. (2003) XANES calibrations for the oxidation state of iron in a silicate glass. *Am. Mineral.* **88**, 967–977.

Bonneville S., Morgan D. J., Schmalenberger A., Bray A., Brown A., Banwart S. A. and Benning L. G. (2011) Tree-mycorrhiza symbiosis accelerate mineral weathering: evidences from nanometer-scale elemental fluxes at the hypha–mineral interface. *Geochim. Cosmochim. Acta* **75**, 6988–7005.

Bonneville S., Smits M. M. and Benning L. G. (2016) Plant-driven fungal weathering: early stages of mineral alteration at the nanometer scale. *Geology* **37**, 615–618.

Cornell R. M. and Schwertmann U. (2004) *The Iron Oxides: Structure, Properties, Reactions, Occurences and Uses.* Wiley-VCH Verlag GmbH & Co, KGaA.

Diaz J. M., Hansel C. M., Voelker B. M., Mendes C. M., Andeer P. F. and Zhang T. (2013) Widespread production of extracellular superoxide by heterotrophic bacteria. *Science* **340**, 1223–1226.

Fujii M., Rose A. L., Omura T. and Waite T. D. (2010) Effect of Fe (II) and Fe(III) transformation kinetics on iron acquisition by a toxic strain of *Microcystis aeruginosa*. *Environ. Sci. Technol.* **44**, 1980–1986.

Gauger T., Konhauser K. and Kappler A. (2015) Protection of phototrophic iron(II)-oxidizing bacteria from UV irradiation by biogenic iron(III) minerals: Implications for early Archean banded iron formation. *Geology* **43**, 1067–1070.

Garcia-Prieto A., Alonso J., Munoz D., Marcano L., Diaz Aba, de Cerio A., Fernandez de Luis R., Orue I., Mathon O., Muela A. and Fdez-Gubieda M. L. (2016) On the mineral core of ferritin-like proteins: structural and magnetic characterization. *Nanoscale* **8**, 1088–1099.

Garrido-Ramírez E. G., Theng B. K. G. and Mora M. L. (2010) Clays and oxide minerals as catalysts and nanocatalysts in Fenton-like reactions – a review. *Appl. Clay Sci.* **47**, 182–192.

Gazzè S. A., Saccone L., Vala Ragnarsdottir K., Smits M. M., Duran A. L., Leake J. R., Banwart S. A. and McMaster T. J. (2012) Nanoscale channels on ectomycorrhizal-colonized chlorite: evidence for plant-driven fungal dissolution. *J. Geophys. Res.: Biogeosci.* **117**, G00N09.

Georgiou C. D., Sun H. J., McKay C. P., Grintzalis K., Papapostolou I., Zisimopoulos D., Panagiotidis K., Zhang G., Koutsopoulou E., Christidis G. E. and Margiolaki I. (2015) Evidence for photochemical production of reactive oxygen species in desert soils. *Nat. Commun.* **6**, 7100.

Hansel C. M., Zeiner C. A., Santelli C. M. and Webb S. M. (2012) Mn(II) oxidation by an ascomycete fungus is linked to superoxide production during asexual reproduction. *Proc. Natl. Acad. Sci. USA* **109**, 12621–12625.

Hemingway J. D., Hilton R. G., Hovius N., Eglinton T. I., Haghipour N., Wacker L., Chen M.-C. and Galy V. V. (2018) Microbial oxidation of lithospheric organic carbon in rapidly eroding tropical mountain soils. *Science* **360**, 209–212.

Hunter R. C., Hitchcock A. P., Dynes J. J., Obst M. and Beveridge T. J. (2008) Mapping the speciation of iron in *Pseudomonas aeruginosa* biofilms using scanning transmission X-ray microscopy. *Environ. Sci. Technol.* **42**, 8766–8772.

Jiang H., Xu R., Chen C. C., Yang W., Fan J., Tao X., Song C., Kohmura Y., Xiao T., Wang Y., Fei Y., Ishikawa T., Mao W. L. and Miao J. (2013) Three-dimensional coherent X-ray diffraction imaging of molten iron in mantle olivine at nanoscale resolution. *Phys. Rev. Lett.* **110** 205501.

Jongmans A. G., van Breemen N., Lundström U., van Hees P. A. W., Finlay R. D., Srinivasan M., Unestam T., Giesler R., Melkerud P. A. and Olsson M. (1997) Rock-eating fungi. *Nature* **389**, 682–683.

Li H., Hu S., Polizzotto M. L., Chang X., Shen Q., Ran W. and Yu G. (2016a) Fungal biomineralization of montmorillonite and goethite to short-range-ordered minerals. *Geochim. Cosmochim. Acta* **191**, 17–31.

Li L., Abe Y., Nagasawa Y., Kudo R., Usui N., Imai K., Mashino T., Mochizuki M. and Miyata N. (2004) An HPLC assay of hydroxyl radicals by the hydroxylation reaction of terephthalic acid. *Biomed. Chromatogr.* **18**, 470–474.

Li Z., Liu L., Chen J. and Teng H. H. (2016b) Cellular dissolution at hypha- and spore-mineral interfaces revealing unrecognized mechanisms and scales of fungal weathering. *Geology* **44**, 319–322.

Lin S. S. and Gurol M. D. (1998) Catalytic decomposition of hydrogen peroxide on iron oxide: kinetics, mechanism, and implications. *Environ. Sci. Technol.* **32**, 1417–1423.

Kumara G. H. A. J. J., Hayano K. and Ogiwara K. (2012) Image analysis techniques on evaluation of particle size distribution of gravel. *Int. J. Geomate* **3**, 290–297.

Manceau A., Marcus M. A. and Grangeon S. (2012) Determination of Mn valence states in mixed-valent manganates by XANES spectroscopy. *Am. Mineral.* **97**, 816–827.

McMaster T. J. (2012) Atomic force microscopy of the fungi-mineral interface: applications in mineral dissolution, weathering and biogeochemistry. *Curr. Opin. Biotechnol.* **23**, 562–569.

Melton E. D., Swanner E. D., Behrens S., Schmidt C. and Kappler A. (2014) The interplay of microbially mediated and abiotic reactions in the biogeochemical Fe cycle. *Nat. Rev. Microbiol.* **12**, 797–808.

Op De Beeck M., Troein C., Peterson C., Persson P. and Tunlid A. (2018) Fenton reaction facilitates organic nitrogen acquisition by an ectomycorrhizal fungus. *New Phytol.* **218**, 335–343.

Petigara B. R., Blough N. V. and Mignerey A. C. (2002) Mechanisms of hydrogen peroxide decomposition in soils. *Environ. Sci. Technol.* **36**, 639–645.

Ravel B. and Newville M. (2005) ATHENA, ARTEMIS, HEPHAESTUS: data analysis for X-ray absorption spectroscopy using IFEFFIT. *J. Synchrot. Radiat.* **12**, 537–541.

Rose A. L., Salmon T. P., Lukondeh T., Neilan B. A. and Waite T. D. (2005) Use of superoxide as an electron shuttle for iron acquisition by the marine cyanobacterium *Lyngbya majuscula*. *Environ. Sci. Technol.* **39**, 3708–3715.

Rudnick R. L. and Gao G. (2004) Composition of the continental crust. In *The Crust: Treatise on Geochemistry* (ed. R. L. Rudnick). Elsevier, Amsterdam, The Netherlands, pp. 1–64.

Schwertmann U. and Cornell R. M. (2007) In *Iron Oxides in the Laboratory*. Wiley-VCH Verlag GmbH, Weinheim, pp. 121–134.

Scott B. and Eaton C. J. (2008) Role of reactive oxygen species in fungal cellular differentiations. *Curr. Opin. Microbiol.* **11**, 488–493.

Shi L., Dong H. L., Reguera G., Beyenal H., Lu A. H., Liu J., Yu H.-Q. and Fredrickson J. K. (2016) Extracellular electron transfer mechanisms between microorganisms and minerals. *Nat. Rev. Microbiol.* **14**, 651–662.

Smits M. M., Herrmann A. M., Duane M., Duckworth O. W., Bonneville S., Benning L. G. and Lundström U. (2009) The fungal-mineral interface: challenges and considerations of micro-analytical developments. *Fungal Biol. Rev.* **23**, 122–131.

Sterflinger K. (2000) Fungi as geologic agents. *Geomicrobiol. J.* **17**, 97–124.

Sun F., Polizzotto M. L., Guan D., Wu J., Shen Q., Ran W., Wang B. and Yu G. (2017) Exploring the interactions and binding sites between Cd and functional groups in soil using two-dimensional correlation spectroscopy and synchrotron radiation based spectromicroscopies. *J. Hazard. Mater.* **326**, 18–25.

Tang Y., Zeiner C. A., Santelli C. M. and Hansel C. M. (2013) Fungal oxidative dissolution of the Mn(II)-bearing mineral rhodochrosite and the role of metabolites in manganese oxide formation. *Environ. Microbiol.* **15**, 1063–1077.

Thompson A., Rancourt D. G., Chadwick O. A. and Chorover J. (2011) Iron solid-phase differentiation along a redox gradient in basaltic soils. *Geochim. Cosmochim. Acta* **75**, 119–133.

van Schöll L., Kuyper T. W., Smits M. M., Landeweert R., Hoffland E. and Breemen N. (2008) Rock-eating mycorrhizas: their role in plant nutrition and biogeochemical cycles. *Plant Soil* **303**, 35–47.

Wang X., Dong H., Zeng Q., Xia Q., Zhang L. and Zhou Z. (2017) Reduced iron-containing clay minerals as antibacterial agents. *Environ. Sci. Technol.* **51**, 7639–7647.

Watts R. J., Udell M. D., Kong S. H. and Leung S. W. (1999) Fenton-like soil remediation catalyzed by naturally occurring iron minerals. *Environ. Eng. Sci.* **16**, 93–103.

Wei Z., Hillier S. and Gadd G. M. (2012) Biotransformation of manganese oxides by fungi: solubilization and production of manganese oxalate biominerals. *Environ. Microbiol.* **14**, 1744–1753.

Whitfield J. (2007) Fungal roles in soil ecology: underground networking. *Nature* **449**, 136–138.

Williams L. B., Metge D. W., Eberl D. D., Harvey R. W., Turner A. G., Prapaipong P. and Poret-Peterson A. T. (2011) What makes a natural clay antibacterial? *Environ. Sci. Technol.* **45**, 3768–3773.

Xiao Y., Zhang E., Zhang J., Dai Y., Yang Z., Christensen H. E. M., Ulstrup J. and Zhao F. (2017) Extracellular polymeric substances are transient media for microbial extracellular electron transfer. *Sci. Adv.* **3** e1700623.

Zhang J. (2015) The molecular mechanism of mycoparasitism of the biocontrol strain Trichoderma Guizhouense NJAU 4742: Function research of the neutral metalloproteasenmp1 and reactive oxygen species. Ph.D. Thesis. Nanjing Agricultural University.

Zhang J., Bayram Akcapinar G., Atanasova L., Rahimi M. J., Przylucka A., Yang D., Kubicek C. P., Zhang R., Shen Q. and Druzhinina I. S. (2016) The neutral metallopeptidase NMP1 of *Trichoderma guizhouense* is required for mycotrophy and self-defence. *Environ. Microbiol.* **18**, 580–597.

Zhang X. Z., Xu Z. J., Tai R. Z., Zhen X. J., Wang Y., Guo Z., Yan R., Chang R., Wang B., Li M., Zhao J. and Gao F. (2010) Ratio-contrast imaging of dual-energy absorption for element mapping with a scanning transmission X-ray microscope. *J. Synchrot. Radiat.* **17**, 804–809.

Associate editor: Jon Chorover